metals

MDPI

Article

Microstructural Evolution and Material Flow during Friction Stir Welding of 6013 Aluminum Alloy Studied by the Stop-Action Technique

Alexander Kalinenko [1], Pavel Dolzhenko [1], Sergey Malopheyev [1], Ivan Shishov [2], Vasiliy Mishin [2], Sergey Mironov [1,*] and Rustam Kaibyshev [1]

[1] Laboratory of Mechanical Properties of Nanoscale Materials and Superalloys, Belgorod National Research University, Pobeda 85, 308015 Belgorod, Russia; kalinenko@bsu.edu.ru (A.K.); dolzhenko_p@bsu.edu.ru (P.D.); malofeev@bsu.edu.ru (S.M.); rustam_kaibyshev@bsu.edu.ru (R.K.)

[2] Institute of Machinery, Materials, and Transport, Peter the Great St. Petersburg Polytechnic University, 195251 St. Petersburg, Russia; shishov_ia@spbstu.ru (I.S.); mishin_vv@spbstu.ru (V.M.)

* Correspondence: mironov@bsu.edu.ru; Tel.: +7-4722-585456

Abstract: This work is part of a wide-ranging study aiming to enhance the technology of dissimilar friction-stir welding of aluminum and titanium. In the previous study, a new approach was proposed that provided an exceptionally narrow intermetallic layer. However, an essential disadvantage of this technique was the significant material softening in the aluminum part. Hence, the present work was undertaken in order to obtain insight into microstructural processes and material flow in the aluminum part. To this end, the stop-action technique was applied. It was found that the microstructural evolution included several stages. Specifically, the initial material underwent the discontinuous static recrystallization in the heat-affected zone. With the approach of the rotating tool, the recrystallized grains experienced continuous dynamic recrystallization, which resulted in grain refinement. The subsequent transportation of material around the rotating tool provided no significant alterations in microstructure. This "superplastic-like" character of material flow was attributed to a dynamic balance between grain refinement and grain coarsening. It was also found that the stirred material experienced a secondary deformation induced by the rotating tool shoulder far behind the welding tool. The concomitant microstructural changes were most pronounced at the upper weld surface and gave rise to a fine-grained layer.

Keywords: aluminum alloys; friction-stir welding (FSW); electron backscatter diffraction (EBSD); microstructure; texture

Citation: Kalinenko, A.; Dolzhenko, P.; Malopheyev, S.; Shishov, I.; Mishin, V.; Mironov, S.; Kaibyshev, R. Microstructural Evolution and Material Flow during Friction Stir Welding of 6013 Aluminum Alloy Studied by the Stop-Action Technique. *Metals* **2023**, *13*, 1342. https://doi.org/10.3390/met13081342

Academic Editors: Elvira Oñorbe and Miguel Cervera

Received: 20 June 2023
Revised: 12 July 2023
Accepted: 25 July 2023
Published: 27 July 2023

1. Introduction

Friction-stir welding (FSW) is often considered a very promising technology for the dissimilar joining of aluminum and titanium alloys [1,2]. Being a solid-state technique, it avoids the difficulties associated with the distinctly different thermal properties of these two materials (e.g., [3,4]), thus enabling their sound welding.

On the other hand, it is important to point out that the dissimilar FSW of aluminum and titanium encounters a number of serious problems. Among those, the formation of a brittle intermetallic layer at the joint interface [5–23], the dispersion of the harmful titanium fragments within the aluminum part [5–8,14,15,18,22,24–27], and the extensive abrasion of the FSW tool in the titanium part [28] are of particular concern. To minimize these drawbacks, a new approach has been proposed in previous work [29]. It assumed the lap-welding configuration of a dissimilar joint and was based on the idea of plunging the FSW tool solely into the aluminum part while keeping it as close as possible to the dissimilar interface. It was shown that this technique resulted in an extremely narrow (~0.1 μm) intermetallic layer and avoided both the formation of titanium fragments and tool wear [29]. As a result, the produced joints exhibited excellent mechanical performance [29].

However, an important limitation of the proposed technique was its high sensitivity to heat-input conditions. Specifically, this approach is only feasible at relatively high heat input. Accordingly, FSW at such conditions resulted in essential material softening in the aluminum part of dissimilar joints, which, in turn, led to premature failure in the heat-affected zone [29]. Hence, the further optimization of the proposed approach required thorough microstructural control in the aluminum part. To this end, a fundamental understanding of the underlying microstructural processes is necessary.

In this context, it is worth noting that the "stop-action" technique [30] is known as one of the most effective techniques for microstructural examinations in FSW. This approach involves an emergency stop of the FSW machine during welding and the subsequent immediate quenching of the material near the final tool position. It is believed that the subsequent microstructural examination of this material would reveal the intrinsic characteristics of microstructural evolution and material behavior during FSW. Indeed, the application of the stop-action technique in a number of previous studies [31–59] has significantly contributed to our current understanding of the microstructural aspects of FSW. Particularly, it has been conclusively demonstrated that microstructural evolution during FSW is a relatively complex phenomenon that may involve a combination of geometric recrystallization, continuous recrystallization, and discontinuous recrystallization [31,32,35,37,39–45]. The mutual contribution of these mechanisms to a global process depends on the nature of the welded material (primarily the stacking fault energy [46]) and, perhaps, FSW thermal conditions. Moreover, it has been found that the stir zone microstructure may experience static coarsening [31,35,37,38,40,41,43,47] (or even static recrystallization [46]) during the FSW cooling cycle. With the aid of the stop-action technique, it has also been shown that material flow during FSW is fairly inhomogeneous along the weld thickness [33,34,37,43,48–51]. Specifically, it is normally governed by the tool shoulder at the upper surface of the stir zone and the tool probe in the weld nugget [33,34,37,43,48–51]. This effect may result in a drastic texture gradient in the thickness direction [33,34]. Furthermore, a particularly complex character of material flow was also observed near the threads of the welding tool [42,52–54].

To the best of the authors' knowledge, so far, the stop-action technique has never been applied for the examination of Al/Ti dissimilar FSW joints. Thus, to provide comprehensive insight into microstructural processes in the aluminum part of the Al/Ti dissimilar joint, it was employed in the present study. It was expected that the comparatively high-heat-input conditions of FSW in this case might give rise to a specific character of microstructural evolution and material flow. Accordingly, the stop-action experiment may highlight new microstructural aspects of FSW.

2. Materials and Methods

The program materials used in the present study included commercial 6013 aluminum alloy and Ti-6Al-4V titanium alloy. The aluminum alloy was produced by semi-continuous casting using a KREIMA laboratory casting machine. The cast ingot was homogenized at 550 °C for 4 h and then cold rolled to a thickness of 2 mm (≈80% of the total thickness reduction). This material condition is referred to as the *base material* hereafter. Titanium alloy was supplied as 2 mm-thick sheets in a mill-annealed state.

A detailed description of the FSW experiment was provided in the previous work [29]. Briefly, a lap welding geometry was employed, the aluminum part was placed on the upper side of the dissimilar joint, and the welding tool was plunged only into the aluminum part; the distance between the tool tip and the titanium side was maintained at ≈50 μm. FSW was conducted using the AccuStir 1004 FSW machine at a spindle rate of 1100 rpm and a feed rate of 3 inches per minute (≈76.2 mm/min). A conventional welding tool was employed. It was manufactured from tool steel and consisted of a concave-shaped shoulder (12.5 mm in diameter) and an M5-threaded cylindrical probe (1.9 mm in length). A typical convention for FSW geometry was adopted, which included welding direction (WD), normal direction (ND), and transverse direction (TD).

To record the FSW thermal cycle, two K-type thermocouples were placed at the aluminum–titanium interface. To this end, appropriate grooves were machined in the plates to be welded, as shown in the schematic in Supplementary Figure S1. To minimize the measurement error, the thermocouples were set as close as possible to the welding tool on its advancing and retreating sides. The typical weld thermal cycles are shown in Figure 1a. In accordance with expectations, it was characterized by a comparatively high peak temperature (≈500 °C) and a relatively slow cooling rate. It is worth noticing that such thermal conditions were partially associated with the relatively slow heat transfer into the bottom Ti-6Al-4V (which virtually acted as a backing plate).

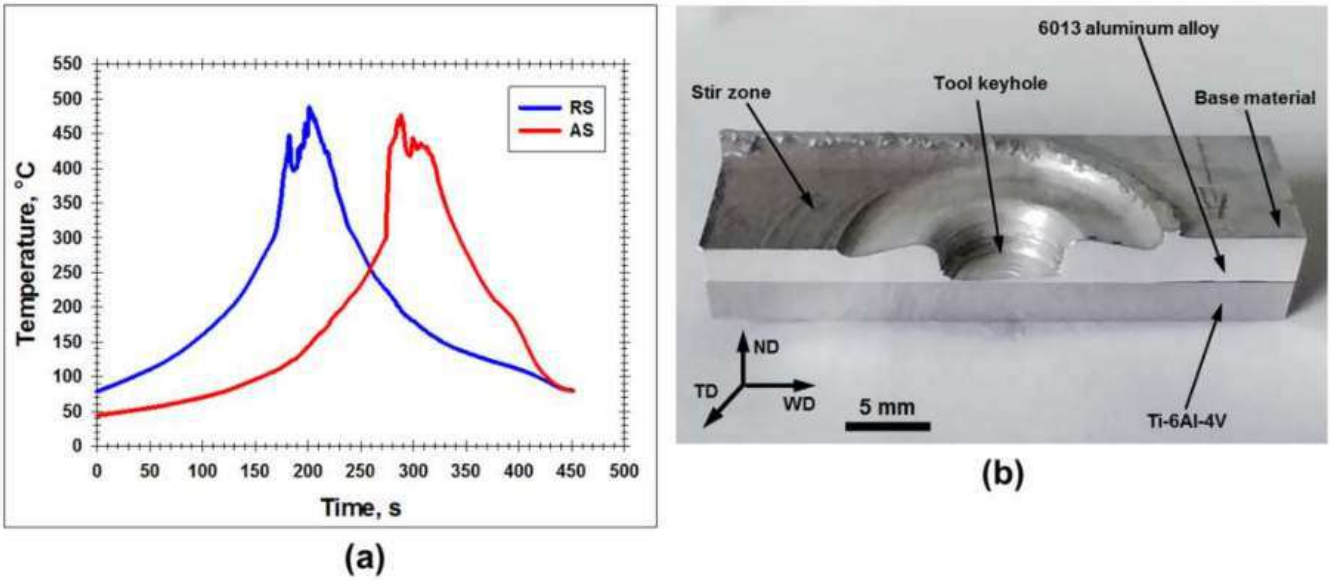

Figure 1. (**a**) The recorded FSW thermal cycle and (**b**) optical image of microstructural sample produced by the stop-action experiment. In (**a**), RS and AS denote the advancing side and retreating side, respectively. In (**b**), WD, ND, and TD are welding direction, normal direction, and transverse direction, respectively.

In order to realize the stop-action experiment, the FSW machine was emergency stopped after traveling ~100 mm, and liquid nitrogen was immediately poured on the final position of the welding tool to "freeze" the FSW-induced microstructure. The subsequent observations showed that the FSW tool was not adhered to the workpiece; therefore, it was gently removed from its keyhole without significant damage to the surrounding material. For microstructural examinations, the final position of the welding tool was sectioned in a longitudinal (WD × ND) plane along the weld centerline, thus permitting a side view of the tool keyhole. The produced microstructural sample is shown in Figure 1b.

Microstructural observations were performed using electron backscatter diffraction (EBSD). To obtain a suitable surface finish, the microstructural sample was mechanically polished in a conventional fashion, with a final step comprising 24 h vibratory polishing with the commercial OP-S suspension.

The EBSD data were collected with an FEI Quanta 600 field-emission-gun scanning electron microscope. It was equipped with TSL OIM^{TM} software and operated at an accelerated voltage of 20 kV. To examine the broad aspects of microstructural evolution and material flow, a series of sample-scale EBSD maps was acquired using a relatively coarse scan step size of 2 μm. For more detailed microstructural analysis in particular areas of interest, higher-resolution maps were also obtained with scan step sizes of 0.5 and 0.2 μm. To improve the fidelity of EBSD data, fine grains comprising either one or two pixels were eliminated from EBSD maps using the standard grain-dilation option of TSL OIM software. A 15-degree criterion was applied to differentiate low-angle boundaries (LABs) from high-angle boundaries (HABs). Throughout the manuscript, LABs and HABs

in EBSD maps were depicted as red and black lines, respectively. Given the limited angular accuracy of EBSD, LABs with misorientations below 2° were excluded from consideration. The grain size was measured using the equivalent grain diameter approach [60].

3. Results and Discussion

3.1. Base Material

The representative portion of the EBSD grain-boundary map taken from the base material in the aluminum part is shown in Figure 2a. The base material had a typical cold-rolled microstructure. Specifically, it was dominated by relatively coarse grains that were heavily elongated in the rolling direction and contained a developed LAB substructure.

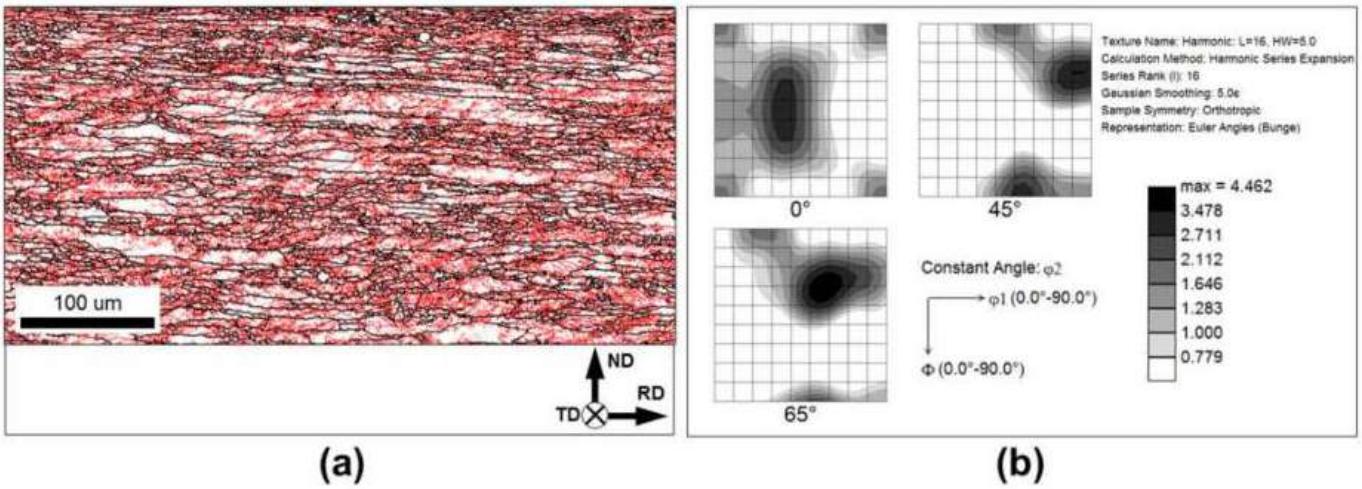

Figure 2. Microstructure and crystallographic texture of base material: (**a**) selected portion of EBSD grain-boundary map and (**b**) $\varphi_2 = 0°$, $\varphi_2 = 45°$, and $\varphi_2 = 65°$ sections of orientation distribution function. In (**a**), LABs and HABs are depicted as red and black lines, respectively; RD, ND and TD are rolling direction, normal direction, and transverse direction, respectively.

To examine crystallographic texture in the base material, orientation data were derived from EBSD maps and arranged as an orientation distribution function (ODF). The selected portions of the ODF were shown in Figure 2b. It is seen that the crystallographic texture exhibited a mixture of typical rolling components with prevalent $S\{123\} < 634 >$ and $Copper\{112\} < 111 >$ orientations and the less pronounced $Brass\{110\} < 112 >$ and $Cube\{001\} < 100 >$ orientations (Figure 2b).

3.2. Microstructural Processes Ahead of the Welding Tool

3.2.1. Grain Structure

To investigate microstructural evolution *ahead* of the welding tool, a sample-scale EBSD grain-boundary map was acquired from this region, as shown in Figure 3. The fairly inhomogeneous microstructure distribution seen in this area evidenced a complicated character of microstructural evolution. In order to provide a closer inspection of this process, a series of higher-resolution maps were taken from particular areas of interest and shown at higher magnification in Figure 4.

Near the outer edge of the FSW-induced zone (location "a" in Figure 3), the initial heavily-rolled microstructure exhibited significant changes. Specifically, an extensive nucleation of the relatively fine equiaxed grains, which contained almost no LAB substructure and were completely outlined by HABs, was revealed (Figure 4a) (the appropriate EBSD grain-orientation-spread map is shown in supplementary Figure S2). From this morphology, this microstructural process appeared to fit the definition of *discontinuous recrystallization*. Remarkably, the recrystallization developed relatively far from the welding tool (Figure 3), and thus it was likely associated with the FSW heat effect rather than with the FSW-induced

strain. If so, the recrystallization was probably *static* in nature, and therefore this microstructural region represented the *heat-affected zone*. The recrystallization in this area was in good agreement with the pronounced material softening observed in the previous work [29].

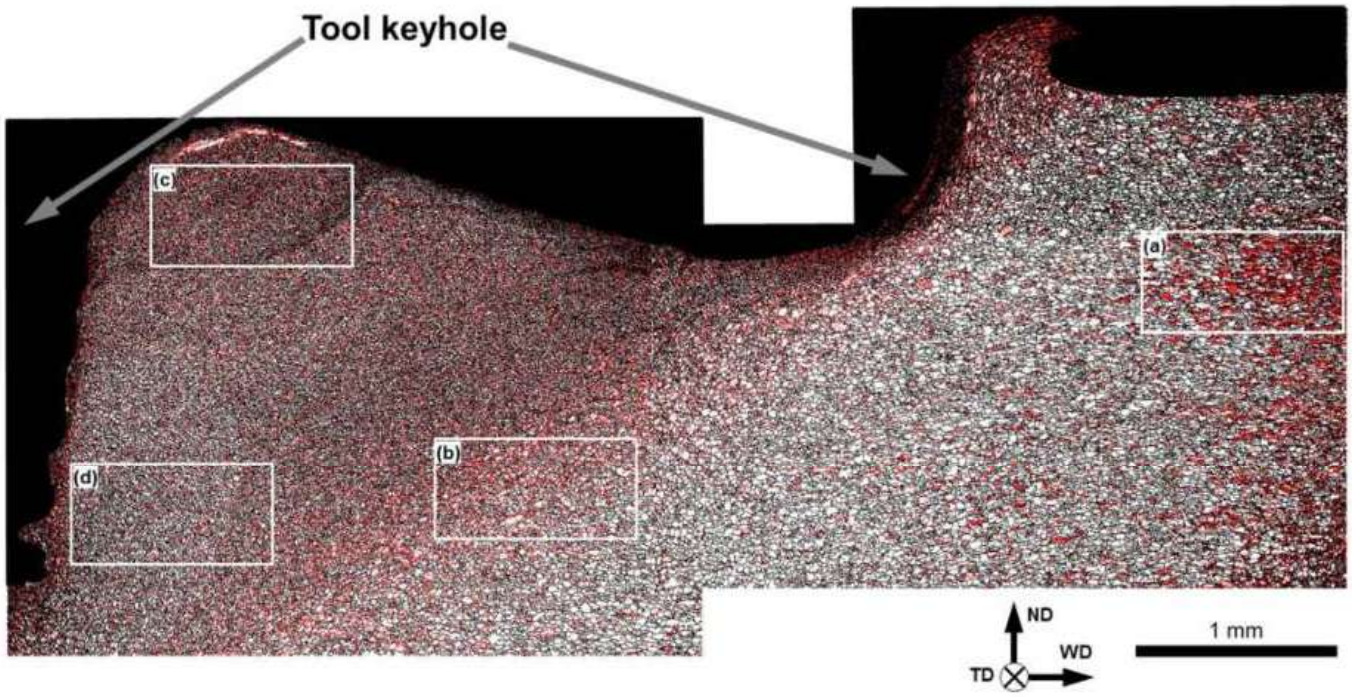

Figure 3. The sample-scale EBSD grain-boundary map showing microstructure evolved *ahead* of welding tool. In the map, LABs and HABs are depicted as red and black lines, respectively. WD, ND and TD are the welding direction, normal direction, and transverse direction, respectively. Note: The labeled selected areas are shown at higher magnification in Figure 4.

With approaching the welding tool (location "b" in Figure 3), the recrystallized grains were sheared/reoriented in a common direction (Figure 4b), thus indicating that the material had experienced a macro-scale strain. Accordingly, this microstructural region could be interpreted as the *thermo-mechanically affected zone*. Within the sheared grains, an extensive formation of LAB substructure was noted, which resulted in a well-developed subgrain structure. In some cases, misorientation of local subboundary segments exceeded 15° thus transforming LABs into HABs, as exemplified by the arrows in Figure 4b. This process promoted the gradual transformation of subgrains into grains, thereby giving rise to grain refinement (Figure 4b). These observations suggested that microstructural evolution in this area was governed by the *continuous recrystallization* mechanism, thus being in broad agreement with a number of previous works in the FSW literature (e.g., [32,35]).

Remarkably, the thermo-mechanically affected zone was relatively wide (Figure 3). This effect was likely attributable to the comparatively high-heat-input condition applied in the present study (Figure 1a), which promoted material softening and thus enhanced its plastic deformation.

Another notable issue was also a distinctly different grain-refinement effect near the tool shoulder and the tool probe (locations "c" and "d" in Figure 3), as compared in Figure 4c and d. This result agreed with some numerical simulation works in FSW (e.g., [61]), which predicted a significant difference in thermal and deformation conditions in these areas. The distinct difference in microstructure between the upper weld surface and the nugget zone has also been reported in a number of experimental works [33,34,37,43,48–51].

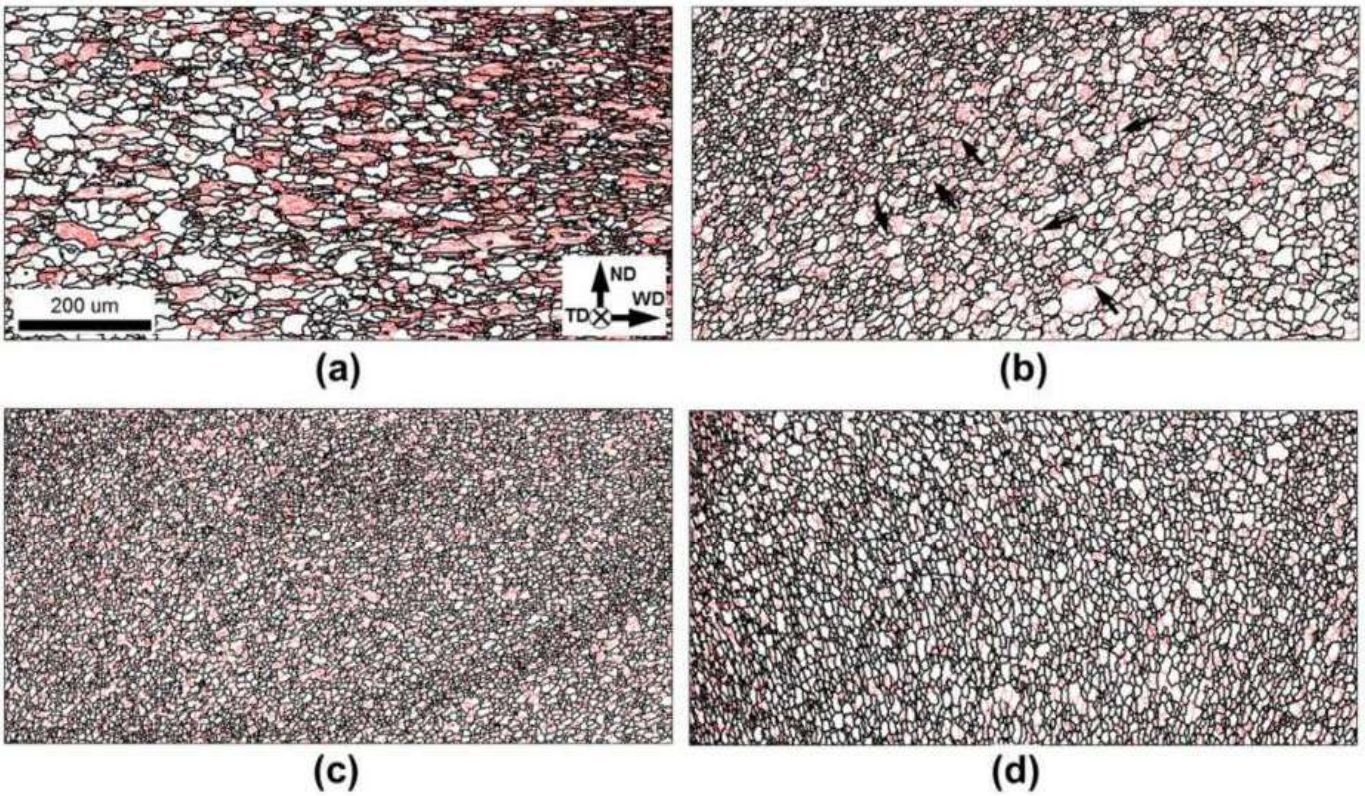

Figure 4. The selected portions of EBSD grain-boundary map in Figure 3 showing microstructure in various microstructural zones: (**a**) heat-affected zone, (**b**) a transition between the heat-affected zone and the thermomechanical-affected zone, (**c**) an area in close proximity to the tool shoulder, and (**d**) an area in close proximity to the tool probe. In all cases, LABs and HABs are depicted as red and black lines, respectively. The scale bar and reference frame for all maps is shown in (**a**). In (**b**), arrows exemplify the gradual LAB-to-HAB transformation (see Section 3.2.1 for details).

3.2.2. Crystallographic Texture

In order to obtain insights into the *crystallographic* aspects of the microstructural processes that occurred ahead of the welding tool, a sample-scale EBSD *orientation* map was obtained, as shown in Figure 5. A distinctly inhomogeneous texture distribution was revealed.

To examine the texture changes in the heat-affected zone, orientation data were extracted from the area labeled "a" in Figure 5, arranged as ODF, and shown in Figure 6a. From the comparison with Figure 2b, it was seen that the initial rolling texture was mainly preserved while becoming more diffusive.

To investigate the texture developed in close proximity to the welding tool, the locations "b" and "c" in Figure 5 were considered. For interpretation of the textural pattern, it is worth noting that material flow during FSW is well accepted to be close to simple shear, with the *shear direction* being tangential to the surface of the welding tool [62]. In the microstructural sample studied in the present work, the shear direction was expected to be opposite the transverse direction ahead of the welding tool, while it should be collinear to the transverse direction behind the welding tool. The orientation of the *shear plane* is less clear in a common case. It is believed that material flow near the weld upper surface is governed by the tool shoulder, and thus the shear plane should be along the shoulder surface [33,34,37,43,48–51]. In the weld nugget, material flow is usually associated with the tool probe, and therefore the shear plane is expected to be nearly parallel to its cylindrical surface [33,34,37,43,48–51]. In view of the above circumstances, the orientation data taken from the friction-stir-welded material typically require an appropriate rotation to align them with the presumed geometry of the simple shear.

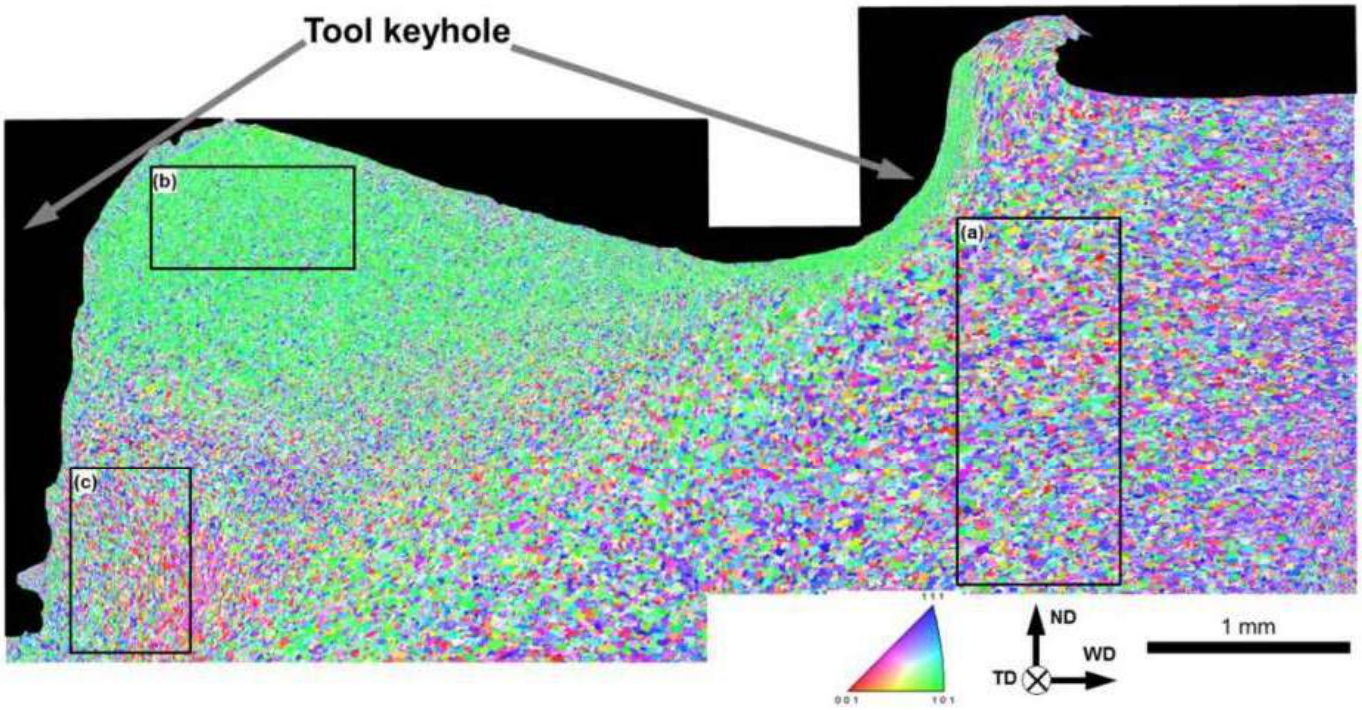

Figure 5. The sample-scale EBSD orientation map showing microstructure that evolved *ahead* of welding tool. In the map, grains are colored according to their crystallographic orientation relative to transverse direction (the orientation color triangle is shown in the bottom part of the figure). WD, ND and TD are the welding direction, normal direction, and transverse direction, respectively. Note: The preferential crystallographic orientations of the selected labelled areas are shown in Figure 6.

Accordingly, the experimental 111 and 110 pole figures measured in the present study were rotated before their analysis. Specifically, to align the horizontal axis of the pole figures with the presumed orientation of shear direction, the pole figures were rotated around the ND. Similarly, to align the vertical axis of the pole figures with the orientation of the shear plane normal, those were rotated around the TD (thus, the rotation around the TD was virtually indicative of the spatial orientation of the shear plane). The rotation angle was selected assuming minimal rotation to reach the nearest simple-shear orientation (to see the ideal simple-shear orientations, which are expected to develop in face-centered cubic crystals (including aluminum), a reader is referred to refs. [62,63]). The rotated pole figures are shown in Figure 6b,c. The applied rotations were indicated in the bottom parts of the figures.

Near the upper surface (location "b" in Figure 5), a reasonable textural pattern was obtained assuming that the shear plane was close to the surface of the concave-shaped shoulder used in the present work; moreover, the texture was dominated by the $B/\overline{B}\{112\} < 110 >$ simple-shear orientation (Figure 6b), which is typically reported in friction-stir-welded aluminum (e.g., [31,32,35]). This result evidenced that material flow in this area was driven by the tool shoulder, in full compliance with expectations.

In the weld nugget (location "c" in Figure 5), the orientation of the shear plane was surprisingly found to be nearly between the shoulder and probe surfaces (Figure 6c). Besides, the texture was comparatively weak (with the peak intensity of the pole figures being only ~2 times random) and diffusive. To a first approximation, this texture could be described in terms of a superposition of $< 110 >$-fiber and $A_1^*/A_2^*\{111\} < 112 >$ simple-shear components. These results are not clear. One of the possible explanations for these observations may be the complex character of material flow in this area due to the influence of the probe threads (Figure 5). This result was consistent with a number of recent works in FSW literature [42,52–54].

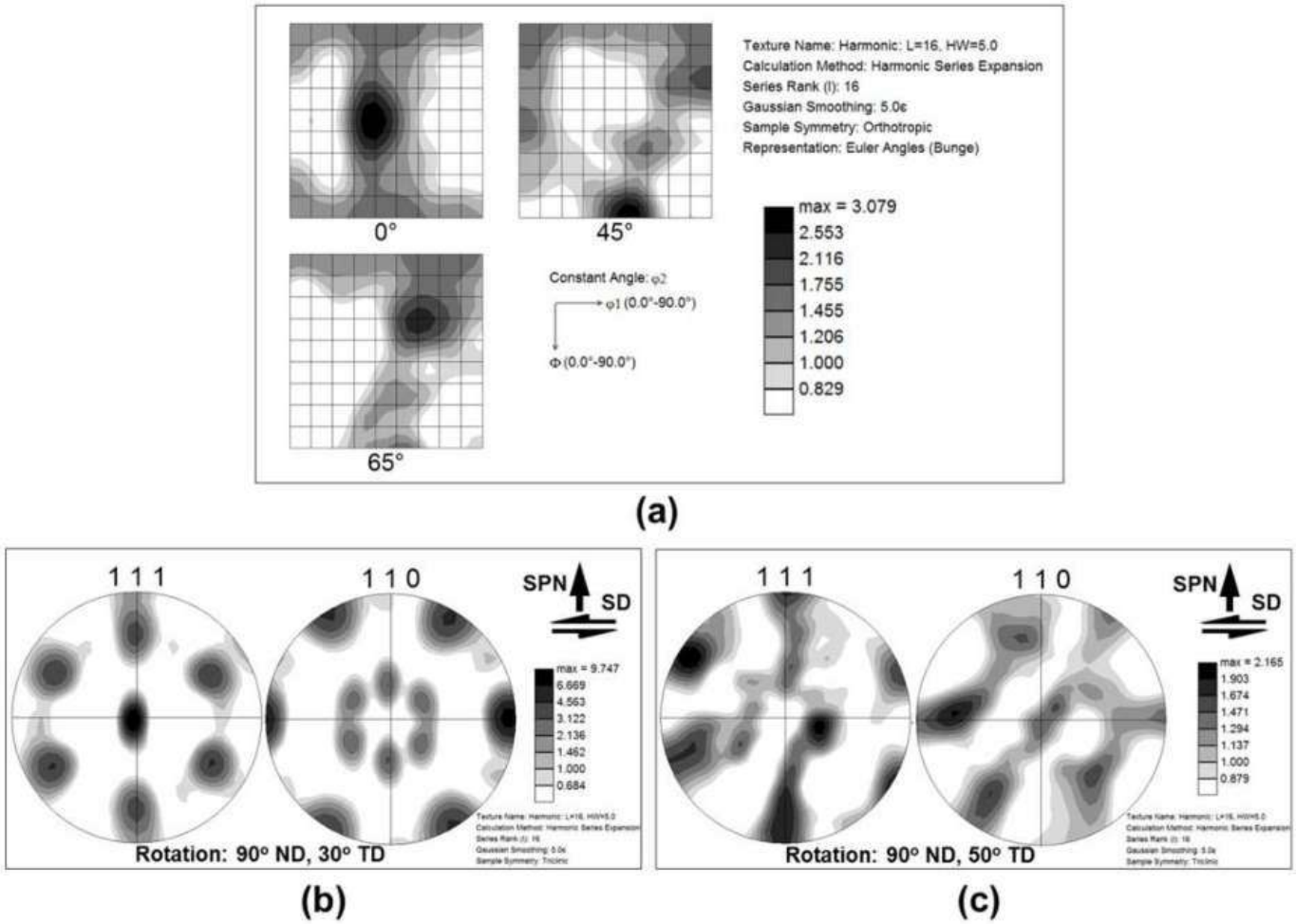

Figure 6. The preferential crystallographic orientations of the selected areas in Figure 5: (**a**) $\varphi_2 = 0°$, $\varphi_2 = 45°$, and $\varphi_2 = 65°$ sections of orientation distribution function showing texture in the heat-affected zone; the 111 and 110 pole figures showing texture in close proximity to (**a**) the tool shoulder, and (**b**) the tool probe. SPN and SD are the shear-plane normal and shear direction, respectively. Note: The pole figures in (**b**,**c**) were appropriately rotated to align them with the local geometry of simple shear; the applied rotations are indicated in the bottom parts of the figures.

3.3. Microstructural Processes behind the Welding Tool

In order to explore the broad aspects of microstructural evolution and material flow *behind* the welding tool, a sample-scale map was taken from this area (Figure 7). A distinctly inhomogeneous microstructure distribution (Figure 7a) and texture distribution (Figure 7b) were revealed. From these observations, it was decided to track microstructural changes in two different regions: (i) near the upper surface of the stir zone (i.e., the shoulder-influenced area) and (ii) the nugget zone (i.e., the probe-influenced area). In each case, three particular locations of interest were selected: (i) in close proximity to the tool probe (locations "a" and "b" in Figure 7a), (ii) near the edge of the tool shoulder (locations "c" and "d" in Figure 7a), and (iii) relatively far from the welding tool (locations "e" and "f" in Figure 7a).

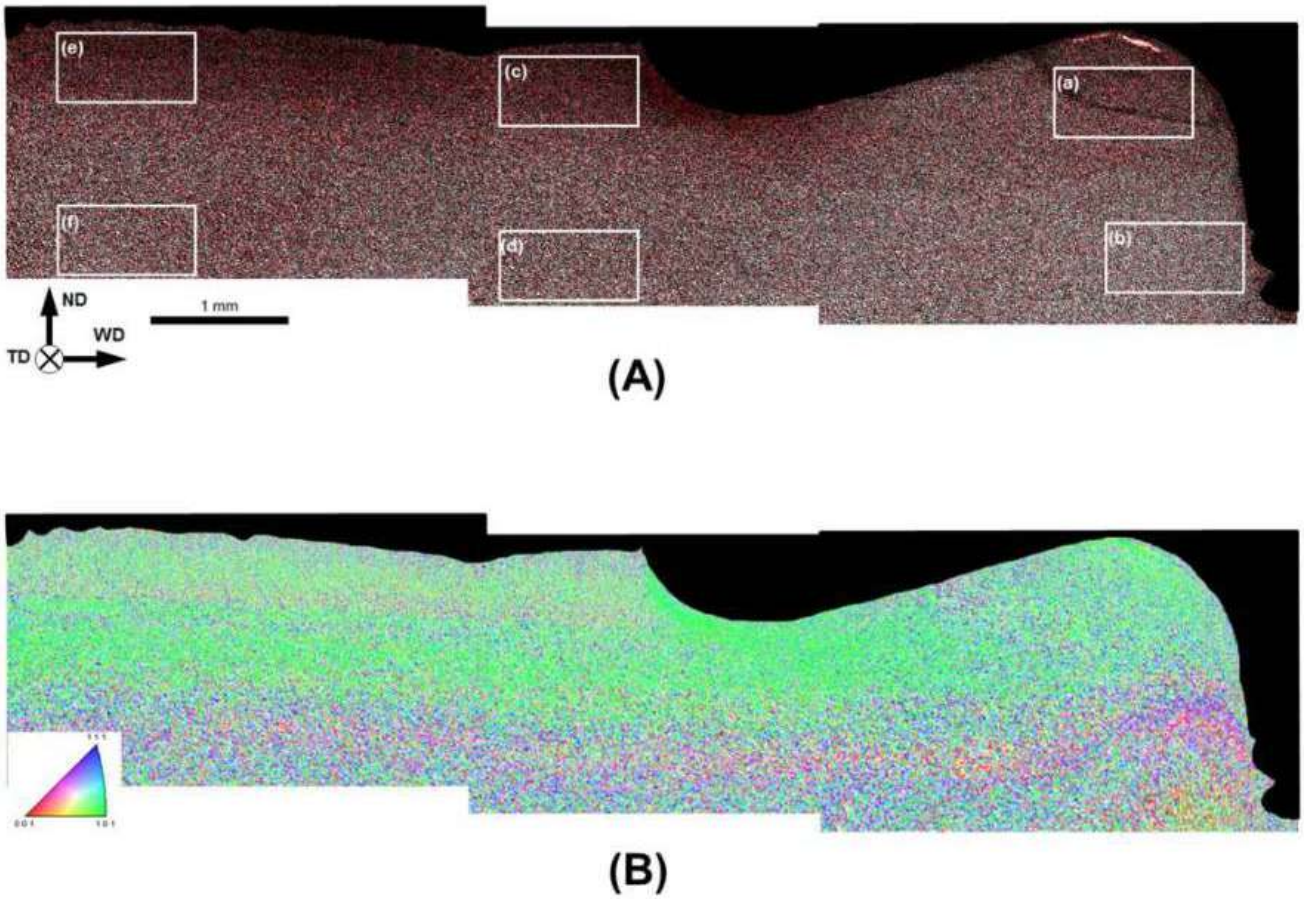

Figure 7. The sample-scale EBSD maps showing microstructure that evolved *behind* the welding tool: (**A**) grain-boundary map and (**B**) orientation map. In (**A**), LABs and HABs are depicted as red and black lines, respectively. In (**B**), grains are colored according to their crystallographic orientation relative to transverse direction (the orientation color triangle is shown in the bottom left corner). WD, ND and TD are the welding direction, normal direction, and transverse direction, respectively. Note: The labeled selected areas in (**A**) are shown at a higher magnification in Figure 8.

3.3.1. Grain-Structure Development

To provide a closer inspection of microstructural changes, high-resolution maps were acquired from the selected areas of interest and given at higher magnification in Figure 8. The grain size statistics derived from the high-resolution maps were shown in Figure 9.

The microstructures that evolved *in close proximity to the welding tool* are presented in Figure 8a,b. One of the most striking issues with these microstructures was their close resemblance to the microstructures revealed in the appropriate locations *ahead* of the tool (compare Figure 8a with Figure 4c, and Figure 8b with Figure 4d). In all cases, microstructures were dominated by the relatively fine, low-aspect-ratio grains, which contained a developed LAB substructure. Statistical analysis revealed only a small difference in grain size between the areas ahead and behind the FSW tool (Figure 9a,b). A broadly similar result has been reported in a number of other stop-action experiments (e.g., [31–34]). Nevertheless, this observation was not entirely trivial. From simple considerations, it seems that the welded material should experience the largest plastic strain during its transportation around the rotating probe. Hence, the subtle microstructural changes during this stage suggest a "superplastic" character of material flow. This observation was likely attributable to the high-heat-input condition of FSW employed in the present study. Such material flow implied either a dynamic balance between grain refinement and grain coarsening or the activation of grain-boundary sliding.

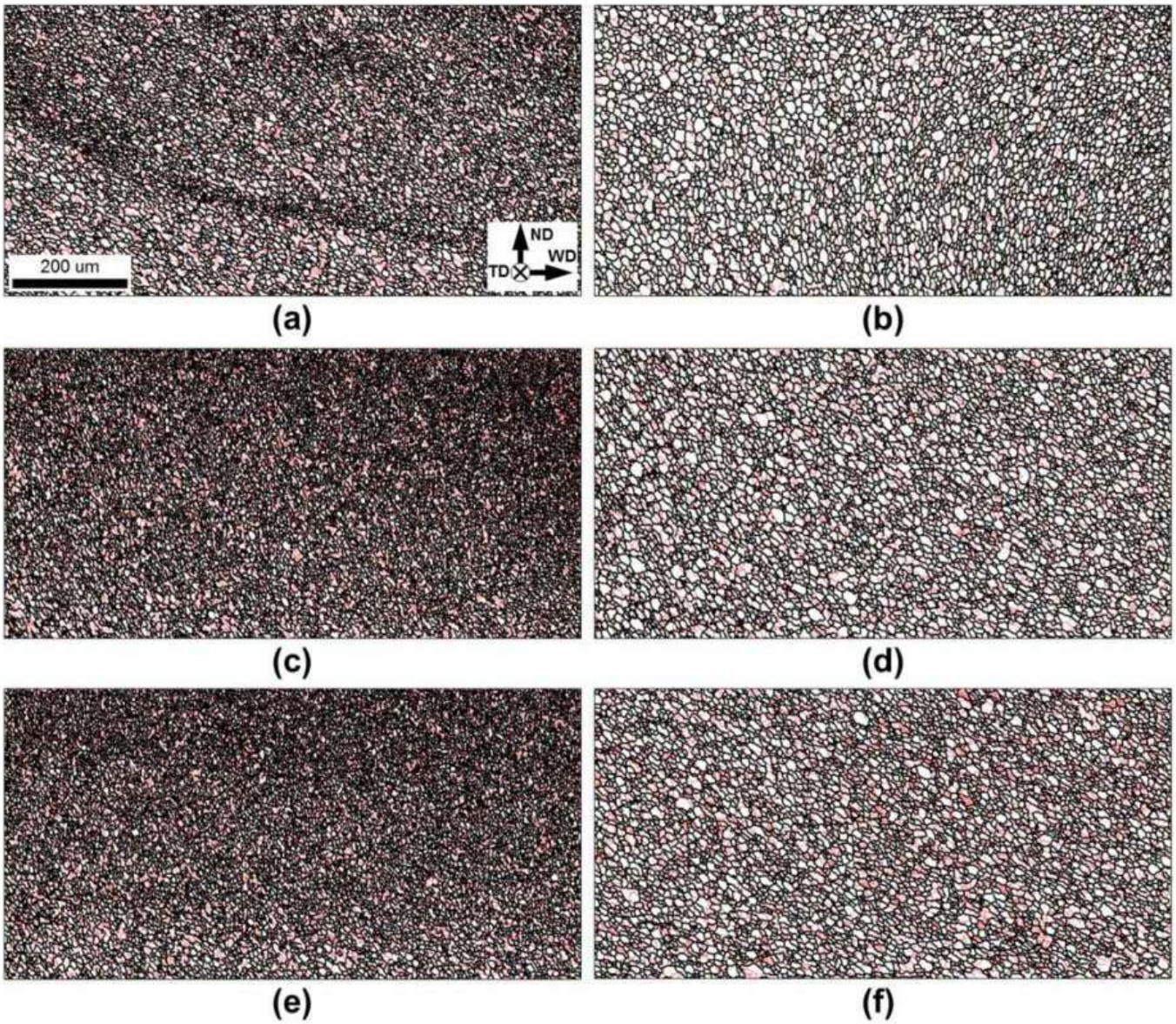

Figure 8. The selected portions of EBSD grain-boundary map in Figure 7a showing microstructures in various microstructural zones behind the welding tool. In all cases, LABs and HABs are depicted as red and black lines, respectively. The scale bar and reference frame for all maps is shown in (**a**). See Section 3.3.1 for details.

The microstructures that developed near the *edge of the tool shoulder* were shown in Figure 8c,d. At the upper surface of the stir zone, an essential grain refinement was found (compare Figure 8a with Figure 8c, Figure 9a). This effect was likely attributable to the secondary deformation exerted by the tool shoulder. Therefore, this result was in excellent accordance with the recent predictions from the numerical simulation of FSW [61]. On the other hand, no significant microstructural changes were observed in the nugget zone (compare Figure 8b with Figures 8d and 9b).

The *final* microstructures produced in the stir zone are shown in Figure 8e,f. In the surface layer, a subtle grain growth was noted (Figure 9a). This observation was likely attributable to the relatively low cooling rate after FSW (Figure 1a), which promoted microstructural coarsening of the stir zone microstructure upon its cooling down to ambient temperature. A broadly similar result has been reported in a number of previous works in the FSW literature [31,35,37,38,40,41,43,47]. In the nugget zone, no significant changes were found (compare Figure 8d with Figures 8e and 9b). The difference in the cooling behavior

of the material in this region was presumably associated with the heat sink into the backing plate (i.e., Ti-6Al-4V).

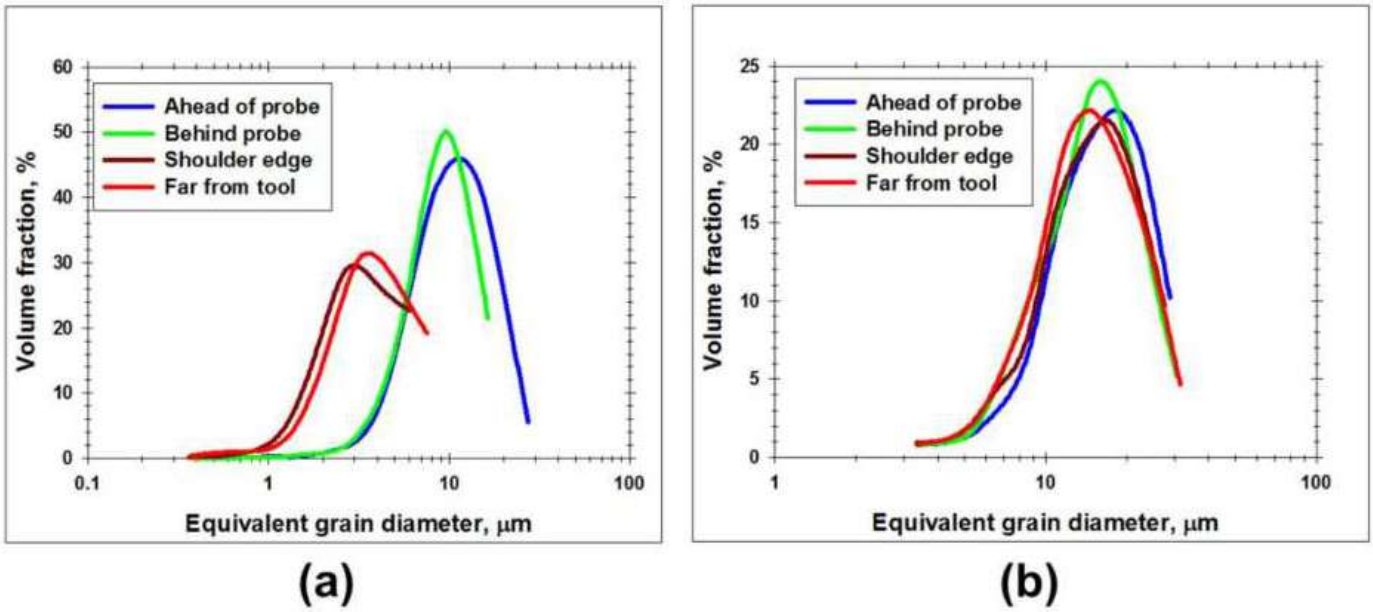

Figure 9. Evolution of grain size distribution as a function of a particular location relative to the welding tool: (**a**) in the upper part of the stir zone and (**b**) in the nugget zone. Note: The grain size data were derived from EBSD maps shown in Figure 8.

The subtle character of the grain coarsening provided the retention of the fine-grained microstructure in the stir zone. This result was consistent with the relatively high hardness in this area, as revealed in the previous study [29].

3.3.2. Evolution of Crystallographic Texture

To investigate texture changes behind the welding tool, orientation data were extracted from the EBSD maps in Figure 8a. Those were arranged as 111 and 110 pole figures, appropriately rotated, and shown in Figures 10 and 11.

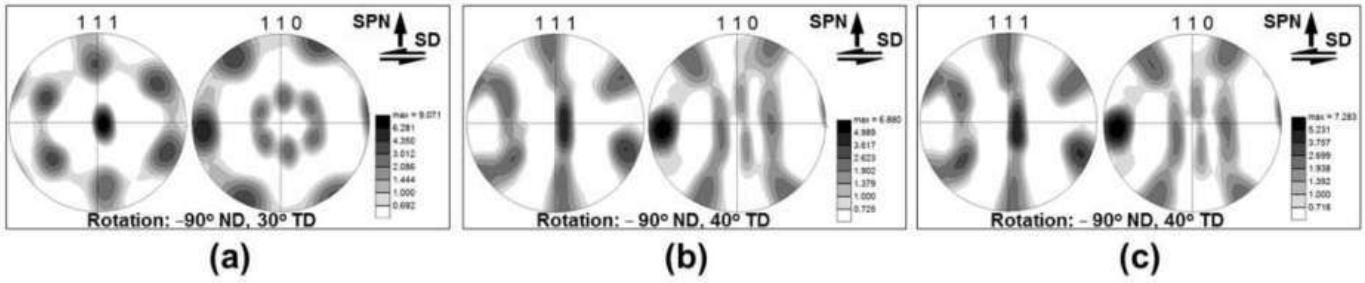

Figure 10. 111 and 110 pole figures showing the evolution of the crystallographic texture in the *upper section* of the stir zone as a function of a particular location behind the welding tool: (**a**) the close proximity to the tool probe (location "a" in Figure 7a), (**b**) near the shoulder edge (location "c" in Figure 7a), and (**c**) far from the welding tool (location "e" in Figure 7a). Note: The pole figures were appropriately rotated to align them with the local geometry of simple shear; the applied rotations are indicated in the bottom parts of the figures. See Section 3.3.2 for details.

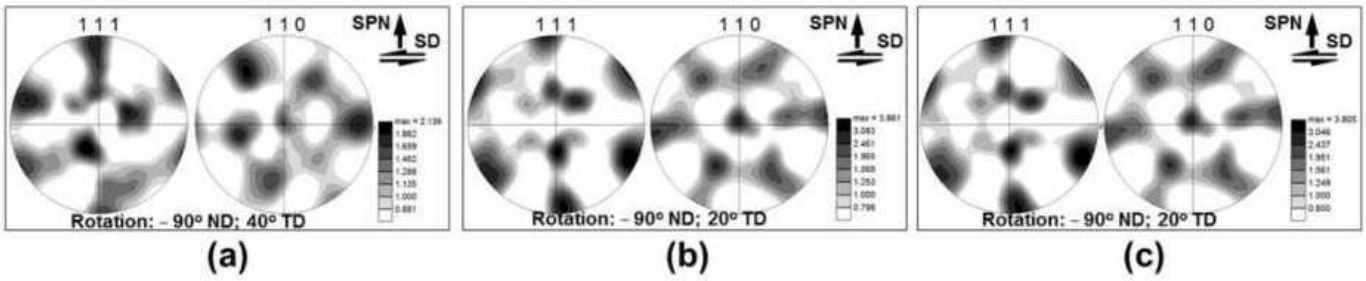

Figure 11. 111 and 110 pole figures showing the evolution of the crystallographic texture in the *nugget zone* as a function of a particular location behind the welding tool: (**a**) the close proximity to the tool probe (location "b" in Figure 7a), (**b**) near the shoulder edge (location "d" in Figure 7a), and (**c**) far from the welding tool (location "f" in Figure 7a). Note: The pole figures were appropriately rotated to align them with the local geometry of simple shear; the applied rotations are indicated in the bottom parts of the figures. See Section 3.3.2 for details.

The textures measured in *close proximity to the tool probe* (locations "a" and "b" in Figure 7a) were found to be broadly similar to the textures revealed ahead of the tool (compare Figures 10a and 6b, and Figures 11a and 6c). The texture invariance was in line with the subtle microstructural changes during transportation of the welded material around the rotating probe, as discussed in the previous section. Hence, this finding was compatible with the presumed "superplastic" character of material flow during this stage. In this context, it is worth noticing that the texture developed at the upper surface layer was relatively strong, with the peak intensity of the pole figures reaching ≈9 times random (Figure 10a). This observation was not entirely consistent with the operation of grain-boundary sliding, thus perhaps excluding this hypothesis from consideration. Therefore, the revealed microstructural stability during material flow around the tool probe was likely a result of a dynamic balance between various microstructural processes, which mutually compensated each other.

Near the *edge of the tool shoulder* (locations "c" and "d" in Figure 7a), significant changes in texture were found. At the *upper surface layer*, the $B/\overline{B}\{112\} < 110 >$ component had transformed into $< 110 >$ fiber; moreover, a significant reduction in texture intensity was revealed (Figure 10b). These observations were in excellent agreement with grain refinement in this area (Figure 9a), thus additionally confirming the secondary deformation experienced by the stir zone material in this area.

In the *nugget zone*, a development of the additional $C\{001\} < 110 >$ texture component was found, and a substantial texture strengthening was noted (Figure 11b). Further, it was also found that the orientation of the shear plane shifted towards the shoulder surface (Figure 11b). All these results evidenced that the material in the nugget zone also experienced the secondary strain.

With a further increase in distance behind the welding tool (locations "e" and "f" in Figure 7a), no substantial alterations in texture pattern were found (compare Figure 10b,c and Figure 11b,c). This perhaps implied that the weld cooling cycle exerted only a minor influence on the *final* texture.

4. Summary

In this work, the stop-action technique was applied to investigate the microstructural evolution and material flow occurring in the aluminum part during dissimilar friction-stir lap welding of 6013 aluminum alloy and Ti-6Al-4V. From extensive EBSD measurements, the following pattern of these processes was derived.

(1) Due to the relatively high-heat-input condition of FSW, the base cold-rolled material first experienced a static recrystallization in the heat-affected zone far ahead of the welding tool. The recrystallization involved the nucleation and growth of recrystallized grains, thus being discontinuous in nature.

(2) With the approach of the welding tool, the recrystallized grains underwent a plastic deformation in the FSW-induced strain field. The extensive development of deformation-induced boundaries gave rise to continuous dynamic recrystallization, which promoted microstructural refinement. The width of the thermo-mechanically affected zone ahead of the welding tool exceeded ~1 mm, thus being relatively broad.

(3) Given the considerable differences in grain size and crystallographic texture, two distinctly different subareas within the thermo-mechanically affected zone were defined, viz., (i) its upper part (i.e., the shoulder-influenced area) and (ii) the nugget zone (i.e., the probe-influenced area). The shoulder-influenced area was characterized by a smaller grain size and a sharper crystallographic texture. The diffuse texture in the nugget zone was attributed to the complex character of material flow in this area due to the influence of the probe threads.

(4) The transportation of the entrapped material around the rotating tool resulted only in minor changes in microstructure, thus evidencing a "superplastic-like" character of material flow. This observation was likely attributable to the high-heat-input condition of FSW employed in the present study. The preservation of the relatively strong crystallographic texture at this stage allowed excluding the grain-boundary sliding from consideration as the key microstructural mechanism. Hence, the revealed microstructural stability was attributed to a dynamic balance between different microstructural processes that mutually compensated each other.

(5) Near the edge of the tool shoulder behind the welding tool, significant changes in microstructure and crystallographic texture were found. These observations evidenced that the stir zone material experienced a secondary deformation due to the stirring action of the tool shoulder. The secondary deformation resulted in the development of a fine-grained surface layer in the stir zone.

Supplementary Materials: The following supporting information can be downloaded at https://www.mdpi.com/article/10.3390/met13081342/s1.

Author Contributions: Conceptualization, S.M. (Sergey Mironov); methodology, A.K., P.D. and S.M. (Sergey Malopheyev); software, S.M. (Sergey Mironov); validation, A.K. and S.M. (Sergey Mironov); formal analysis, S.M. (Sergey Mironov); investigation, A.K., P.D., S.M. (Sergey Malopheyev) and S.M. (Sergey Mironov); resources, R.K.; data curation, S.M. (Sergey Mironov); writing—original draft preparation, S.M. (Sergey Mironov); writing—review and editing, A.K., P.D., S.M. (Sergey Malopheyev), I.S., V.M. and R.K.; visualization, S.M. (Sergey Mironov); supervision, R.K.; project administration, S.M. (Sergey Mironov). All authors have read and agreed to the published version of the manuscript.

Funding: This research was funded by the Russian Science Foundation, grant No. 22-49-04401.

Data Availability Statement: Data will be made available on request.

Acknowledgments: The experimental work was performed using the equipment of the Research Equipment Sharing Center "Technology and Materials" at Belgorod National Research University (financial support from the Ministry of Science and Higher Education of the Russian Federation under the agreement No. 075-15-2021-690, the unique project identifier RF 2296.61321X0030).

Conflicts of Interest: The authors declare no conflict of interest.

References

1. Simar, A.; Avettand-Fenoel, M.-N. State of the Art about Dissimilar Metal Friction Stir Welding. *Sci. Technol. Weld. Join.* **2017**, *22*, 389–403. [CrossRef]
2. Shankar, S.; Mehta, K.P.; Chattopadhyaya, S.; Vilaca, P. Dissimilar Friction Stir Welding of Al to non-Al Metallic Materials: An overview. *Mater. Chem. Phys.* **2022**, *288*, 126371. [CrossRef]
3. Xue, X.; Wu, X.; Liao, J. Hot Cracking Susceptibility and Shear Fracture Behavior of Dissimilar Ti6Al4V/AA6060 Alloys in Pulsed Nd:YAG Laser Welding. *Chin. J. Aeronaut.* **2021**, *34*, 375–386. [CrossRef]
4. Xue, X.; Pereira, A.; Vincze, G.; Wu, X.; Liao, J. Interfacial Characteristics of Dissimilar Ti6Al4V/AA6060 Lap Joint by Pulsed Nd:YAG Laser Welding. *Metals* **2019**, *9*, 71. [CrossRef]

5. Pereira, V.F.; Fonseca, E.B.; Costa, A.M.S.; Bettini, J.; Lopes, E.S.N. Nanocrystalline Structural Layer Acts as Interfacial Bond in Ti/Al Dissimilar Joints Produced by Friction Stir Welding in Power Control Mode. *Scr. Mater.* **2020**, *174*, 80–86. [CrossRef]
6. Choi, J.-W.; Liu, H.; Fujii, H. Dissimilar Friction Stir Welding of Pure Ti and Pure Al. *Mater. Sci. Eng. A* **2018**, *730*, 168–176. [CrossRef]
7. Kar, A.; Suwas, S.; Kailas, S.V. Two-Pass Friction Stir Welding of Aluminum Alloy to Titanium Alloy: A Simultaneous Improvement in Mechanical Properties. *Mater. Sci. Eng. A* **2018**, *733*, 199–210. [CrossRef]
8. Li, B.; Shen, Y.; Luo, L.; Hu, W. Effects of Processing Variables and Heat Treatments on Al/Ti-6Al-4V Interface Microstructure of Bimetal Clad-Plate Fabricated via a Novel Route Employing Friction Stir Lap Welding. *J. Alloys Compd.* **2016**, *658*, 904–913. [CrossRef]
9. Zhao, H.; Yu, M.; Jiang, Z.; Zhou, L.; Song, X. Interfacial Microstructure and Mechanical Properties of Al/Ti Dissimilar Joints Fabricated via Friction Stir Welding. *J. Alloys Compd.* **2019**, *789*, 139–149. [CrossRef]
10. Huang, Y.; Lv, Z.; Wan, L.; Shen, J.; dos Santos, J.F. A new Method of Hybrid Friction Sir Welding Assisted by Friction Surfacing for Joining Dissimilar Ti/Al alloy. *Mater. Lett.* **2017**, *207*, 172–175. [CrossRef]
11. Wu, A.; Song, Z.; Nakata, K.; Liao, J.; Zhou, L. Interface and Properties of the Friction Stir Welded Joints of Titanium Alloy Ti6Al4V with Aluminum Alloy 6061. *Mater. Des.* **2015**, *71*, 85–92. [CrossRef]
12. Aonuma, M.; Nakata, K. Dissimilar Metal Joining of 2024 and 7075 Aluminum Alloys to Titanium Alloys by Friction Stir Welding. *Mater. Trans.* **2011**, *52*, 948–952. [CrossRef]
13. Yu, M.; Zhao, H.; Jiang, Z.; Guo, F.; Zhou, L.; Song, X. Microstructure and Mechanical Properties of Friction Stir Lap AA6061-Ti6Al4V Welds. *J. Mater. Proc. Technol.* **2019**, *270*, 274–284. [CrossRef]
14. Kar, A.; Kailas, S.V.; Suwas, S. Effect of Zinc Interlayer in Microstructure Evolution and Mechanical Properties in Dissimilar Friction Stir Welding of Aluminum to Titanium. *J. Mater. Eng. Perform.* **2018**, *27*, 6016–6026. [CrossRef]
15. Shehabeldeen, T.A.; Yin, Y.; Ji, X.; Shen, X.; Zhang, Z.; Zhou, J. Investigation of the Microstructure, Mechanical Properties and Fracture Mechanisms of Dissimilar Friction Stir Welded Aluminium/Titanium Joints. *J. Mater. Res. Technol.* **2021**, *11*, 507–518. [CrossRef]
16. Kar, A.; Suwas, S.; Kailas, S.V. Significance of Tool Offset and Copper Interlayer during Friction Stir Welding of Aluminum to Titanium. *Int. J. Adv. Manuf. Technol.* **2019**, *100*, 435–443. [CrossRef]
17. Zhou, L.; Yu, M.; Zhao, H.; Jiang, Z.; Guo, F.; Song, X. Dissimilar Friction Stir Welding of AA6061 and Ti6Al4V Alloys: A study on Microstructure and Mechanical Properties. *J. Manuf. Proc.* **2019**, *48*, 119–126. [CrossRef]
18. Chen, Y.; Yu, L.; Ni, Q. Influence of Zinc on the Microstructure and Brittle Phases of Friction Stir Welded Joint of Al/Ti Dissimilar Alloys. *Adv. Mater. Res.* **2012**, *413*, 439–443. [CrossRef]
19. Kar, A.; Kailas, S.V.; Suwas, S. Effect of Mechanical Mixing in Dissimilar Friction Stir Welding of Aluminum to Titanium with Zinc Interlayer. *Trans. Ind. Inst. Met.* **2019**, *72*, 1533–1536. [CrossRef]
20. Nasir, T.; Kalaf, O.; Asmael, M.; Zeeshan, Q.; Safaei, B.; Hussain, G.; Motallebzadeh, A. The Experimental Study of CFRP Interlayer of Dissimilar Joint AA7075-T651/T-6Al-4V Alloys by Friction Stir Spot Welding on Mechanical and Microstructural Properties. *Nanotechnol. Rev.* **2021**, *10*, 401–413. [CrossRef]
21. Chen, Z.W.; Yazdanian, S. Microstructures in Interface Region and Mechanical Behaviours of Friction Stir Lap Al6060 to Ti–6Al–4V welds. *Mater. Sci. Eng. A* **2015**, *634*, 37–45. [CrossRef]
22. Dressler, U.; Biallas, G.; Mercado, U.A. Friction Stir Welding of Titanium Alloy TiAl6V4 to Aluminium Alloy AA2024-T3. *Mater. Sci. Eng. A* **2009**, *526*, 113–117. [CrossRef]
23. Yu, M.; Zhao, H.; Xu, F.; Chen, T.; Zhou, L.; Song, X.; Ma, N. Effects of Ultrasonic on Friction stir Al–Ti Welds: A Comparative Study. *Sci. Technol. Weld. Join.* **2021**, *26*, 551–558. [CrossRef]
24. Kar, A.; Yadav, D.; Suwas, S.; Kailas, S.V. Role of Plastic Deformation Mechanisms during the Microstructural Evolution and Intermetallics Formation in Dissimilar Friction Stir Weld. *Mater. Character.* **2020**, *164*, 110371. [CrossRef]
25. Kar, A.; Malopheyev, S.; Mironov, S.; Kaibyshev, R.; Suwas, S.; Kailas, S.V. A New Method to Elucidate Fracture Mechanism and Microstructure Evolution in Titanium during Dissimilar Friction Stir Welding of Aluminum and Titanium. *Mater. Character.* **2021**, *171*, 110791. [CrossRef]
26. Kar, A.; Suwas, S.; Kailas, S.V. Multi-Length Scale Characterization of Microstructure Evolution and its Consequence on Mechanical Properties in Dissimilar Friction Stir Welding of Titanium to Aluminum. *Metall. Mater. Trans. A* **2019**, *50*, 5153–5173. [CrossRef]
27. Ma, Z.; Sun, X.; Ji, S.; Wang, Y.; Yue, Y. Influences of Ultrasonic on Friction Stir Welding of Al/Ti Dissimilar Alloys Under Different Welding Conditions. *Int. J. Adv. Manuf. Technol.* **2021**, *112*, 2573–2582. [CrossRef]
28. Mironov, S.; Sato, Y.S.; Kokawa, H. Friction-stir welding and Processing of Ti-6Al-4V Titanium alloy: A Review. *J. Mater. Sci. Technol.* **2018**, *34*, 58–72. [CrossRef]
29. Kalinenko, A.; Dolzhenko, P.; Borisova, Y.; Malopheyev, S.; Mironov, S.; Kaibyshev, R. Tailoring of Dissimilar Friction Stir Lap Welding of Aluminum and Titanium. *Materials* **2022**, *15*, 8418. [CrossRef]
30. Colligan, K. Material Flow Behavior during Friction Stir Welding of Aluminum. *Weld. J.* **1999**, *78*, 229–237.
31. Prangnell, P.B.; Heason, C.P. Grain Structure Formation during Friction Stir Welding Observed by the 'Stop Action Technique'. *Acta Mater.* **2005**, *53*, 3179–3192. [CrossRef]

32. Fonda, R.W.; Bingert, J.F.; Colligan, K.J. Development of Grain Structure during Friction Stir Welding. *Scr. Mater.* **2004**, *51*, 243–248. [CrossRef]
33. Suhuddin, U.F.H.R.; Mironov, S.; Sato, Y.S.; Kokawa, H.; Lee, C.-W. Grain Structure Evolution during Friction-Stir Welding of AZ31 Magnesium Alloy. *Acta Mater.* **2009**, *57*, 5406–5418. [CrossRef]
34. Mironov, S.; Onuma, T.; Sato, Y.S.; Kokawa, H. Microstructure Evolution during Friction-Stir Welding of AZ31 Magnesium Alloy. *Acta Mater.* **2015**, *100*, 301–312. [CrossRef]
35. Suhuddin, U.F.H.R.; Mironov, S.; Sato, Y.S.; Kokawa, H. Grain Structure and Texture Evolution during Friction Stir Welding of Thin 6016 Aluminum Alloy Sheets. *Mater. Sci. Eng. A* **2010**, *527*, 1962–1969. [CrossRef]
36. Liu, F.C.; Nelson, T.W. In-Situ Grain Structure and Texture Evolution during Friction Stir Welding of Austenite Stainless Steel. *Mater. Design.* **2017**, *115*, 467–478. [CrossRef]
37. Liu, X.C.; Sun, Y.F.; Nagira, T.; Ushioda, K.; Fujii, H. Evaluation of Dynamic Development of Grain Structure during Friction Stir Welding of Pure Copper Using a Quasi in Situ Method. *J. Mater. Sci. Technol.* **2019**, *35*, 1412–1421. [CrossRef]
38. Mahto, R.P.; Rout, M.; Pal, S.K. Mechanism of Microstructure Evolution and Grain Growth in Friction Stir Welding of AA6061-T6 and AISI304 in Air and Water Media. *Mater. Chem. Phys.* **2021**, *273*, 125081. [CrossRef]
39. Chen, J.; Li, Z.; Han, J.; Peng, L.; Fujii, H.; Wu, Y.; Cheng, H. Investigation on Microstructure Evolution of Mg-Gd-Zn-Zr Alloys during Friction Stir Processing by Liquid CO_2 Cooling Assisted Stop Action. *Mater. Sci. Eng. A* **2023**, *876*, 145140. [CrossRef]
40. Liu, X.C.; Sun, Y.F.; Fujii, H. Clarification of Microstructure Evolution of Aluminum during Friction Stir Welding Using Liquid CO_2 Rapid Cooling. *Mater. Design.* **2017**, *129*, 151–163. [CrossRef]
41. Liu, X.C.; Sun, Y.F.; Nagira, T.; Fujii, H. Investigation of Temperature Dependent Microstructure Evolution of Pure Iron during Friction Stir Welding Using Liquid CO_2 Rapid Cooling. *Mater. Character.* **2018**, *137*, 24–38. [CrossRef]
42. Imam, M.; Sun, Y.; Fujii, H.; Ma, N.; Tsutsumi, S.; Ahmed, S.; Chintapenta, V.; Murakawa, H. Deformation Characteristics and Microstructural Evolution in Friction Stir Welding of Thick 5083 Aluminum Alloy. *Int. J. Adv. Manuf. Technol.* **2018**, *99*, 663–681. [CrossRef]
43. Liu, X.C.; Sun, Y.F.; Nagira, T.; Ushioda, K.; Fujii, H. Microstructure Evolution of Cu–30Zn during Friction Stir Welding. *J. Mater. Sci.* **2018**, *53*, 10423–10441. [CrossRef]
44. Xu, N.; Chen, L.; Feng, R.N.; Song, Q.N.; Bao, Y.F. Recrystallization of Cu-30Zn Brass during Friction Stir Welding. *J. Mater. Res. Technol.* **2020**, *9*, 3746–3758. [CrossRef]
45. Nagira, T.; Liu, X.; Ushioda, K.; Fujii, H. Microstructural Evolutions of 2N Grade Pure Al and 4N Grade High-Purity Al during Friction Stir Welding. *Materials* **2021**, *14*, 3606. [CrossRef]
46. Liu, X.; Sun, Y.; Nagira, T.; Ushioda, K.; Fujii, H. Effect of Stacking Fault Energy on the Grain Structure Evolution of FCC Metals during Friction Stir Welding. *Acta Metall. Sin.* **2020**, *33*, 1001–1012. [CrossRef]
47. Xu, N.; Ueji, R.; Fujii, H. Dynamic and Static Change of Grain Size and Texture of Copper during Friction Stir Welding. *J. Mater. Proc. Technol.* **2016**, *232*, 90–99. [CrossRef]
48. Liu, X.C.; Wu, C.S. Elimination of Tunnel Defect in Ultrasonic Vibration Enhanced Friction Stir Welding. *Mater. Design.* **2016**, *90*, 350–358. [CrossRef]
49. Zhang, Z.; Xiao, B.L.; Wang, D.; Ma, Z.Y. Effect of Alclad Layer on Material Flow and Defect Formation in Friction-Stir-Welded 2024 Aluminum Alloy. *Metall. Mater. Trans. A.* **2011**, *42*, 1717–1726. [CrossRef]
50. Liu, X.C.; Sun, Y.F.; Nagira, T.; Ushioda, K.; Fujii, H. Experimental Evaluation of Strain and Strain Rate during Rapid Cooling Friction Stir Welding of Pure Copper. *Sci. Technol. Weld. Join.* **2019**, *24*, 352–359. [CrossRef]
51. Zhang, L.; Wang, X.; Wei, X. Evolution of Grain Structure and Texture for 6082-T6 Aluminum Alloy during Friction Stir Welding. *J. Wuhan Univ. Technol.* **2019**, *34*, 397–403. [CrossRef]
52. Da Silva, A.A.M.; Arruti, E.; Janeiro, G.; Aldanondo, E.; Alvarez, P.; Echeverria, A. Material Flow and Mechanical Behaviour of Dissimilar AA2024-T3 and AA7075-T6 Aluminium Alloys Friction Stir Welds. *Mater. Design.* **2011**, *32*, 2021–2027. [CrossRef]
53. Imam, M.; Sun, Y.; Fujii, H.; Ma, N.; Tsutsumi, S.; Murakawa, H. Microstructural Characteristics and Mechanical Properties of Friction Stir Welded Thick 5083 Aluminum Alloy. *Metall. Mater. Trans. A.* **2017**, *48*, 208–229. [CrossRef]
54. Alvarez, P.; Janeiro, G.; da Silva, A.A.M.; Aldanondo, E.; Echeverria, A. Material Flow and Mixing Patterns during Dissimilar FSW. *Sci. Technol. Weld. Join.* **2010**, *15*, 648–653. [CrossRef]
55. Zeng, X.H.; Xue, P.; Wang, D.; Ni, D.R.; Xiao, B.L.; Wang, K.S.; Ma, Z.Y. Material Flow and Void Defect Formation in Friction Stir Welding of Aluminium alloys. *Sci. Technol. Weld. Join.* **2018**, *23*, 677–686. [CrossRef]
56. Raturi, M.; Bhattacharya, A. Microstructure and Texture Correlation of Secondary Heating Assisted Dissimilar Friction Stir Welds of Aluminum Alloys. *Mater. Sci. Eng. A* **2021**, *825*, 141891. [CrossRef]
57. Gera, D.; Fu, B.; Suhuddin, U.F.H.R.; Plaine, A.; Alcantara, N.; dos Santos, J.F.; Klusemann, B. Microstructure, Mechanical and Functional Properties of Refill Friction Stir Spot Welds on Multilayered Aluminum Foils for Battery Application. *J. Mater. Res. Technol.* **2021**, *13*, 2272–2286. [CrossRef]
58. Li, G.; Zhou, L.; Luo, L.; Wu, X.-M.; Guo, N. Material Flow Behavior and Microstructural Evolution during Refill Friction Stir Spot Welding of Alclad 2A12-T4 Aluminum Alloy. *Int. J. Miner. Metall. Mater.* **2021**, *28*, 131–141. [CrossRef]
59. Yamamoto, H.; Imagawa, Y.; Ito, K.; Chen, K.; Zhang, L. Alloying a Topmost Steel-Plate Layer with WC-Tool Constituent Elements during Friction Stir Processing. *J. Manuf. Proc.* **2021**, *69*, 311–319. [CrossRef]
60. Humphreys, F.J. Quantitative Metallography by Electron Backscatter Diffraction. *J. Micros.* **1999**, *195*, 170–185. [CrossRef]

61. Mishin, V.; Shishov, I.; Kalinenko, A.; Vysotskii, I.; Zuiko, I.; Malopheyev, S.; Mironov, S.; Kaibyshev, R. Numerical Simulation of the Thermo-Mechanical Behavior of 6061 Aluminum Alloy during Friction-Stir Welding. *J. Manuf. Mater. Process.* **2022**, *6*, 68. [CrossRef]
62. Fonda, R.W.; Knipling, K.E. Texture Development in Friction Stir Welds. *Sci. Technol. Weld. Join.* **2011**, *16*, 288–294. [CrossRef]
63. Hou, W.; Ding, Y.; Huang, G.; Huda, N.; Ahmad Shah, L.H.; Piao, Z.; Shen, Y.; Shen, Z.; Gerlich, A. The Role of Pin Eccentricity in Friction Stir Welding of Al-Mg-Si Alloy Sheets: Microstructural Evolution and Mechanical Properties. *Int. J. Adv. Manuf. Technol.* **2022**, *121*, 7661–7675. [CrossRef]